A Quadruple Band-Notched SWB MIMO Antenna with Enhanced Isolation Using Wiggly Line

Abhishek Kumar CHAUDHARY, Murli MANOHAR

Dept. of Electronics and Communication Engineering, IIIT Senapati, Mantripukhri, 795002 Imphal, India

achaudhary@iiitmanipur.ac.in, murli0641@gmail.com

Abstract. *A novel quadruple band-notched spatial diversity/MIMO antenna for super wideband (SWB) application is investigated. The proposed antenna comprises two identical tapered semicircular radiators with two microstrip feedlines and a common slotted ground plane (CSGP), contributing a wide impedance bandwidth from 1.88–30 GHz. Further, a wiggly-line-decoupling-structure (WLDS) is introduced among the radiating ports to maximize the average isolation, more than 24 dB. The first band-notched functionality at 2.4 GHz is produced by etching a meandering slot on the CSGP, while the remaining three notch bands at 3.5, 5.5, and 7.5 GHz are obtained by implanting open-ended-semicircular (OES), complementary-split-ring-resonator (CSRR), and elliptical-split-ring-resonator (ESRR) slots in each radiating patch. The designed and fabricated results for the two and four elements are analyzed, which exhibit wideband characteristics, stable radiation pattern, higher efficiency (above 85%), and reasonably high peak gain within the working frequency, excluding the quadruple notched bands. Moreover, other essential parameters such as ECC, DG, CCL, and TARC have also been analyzed, showing the antenna's usefulness for radar imaging, cognitive radio, military, and long-range RF applications.*

Keywords

Diversity antenna, quadruple band-notch, SWB, tapered semicircular patch, WLDS

1. Introduction

The rising demand for internet of things (IoT)-based electronic devices for home, industry, health, farming, online services, etc., is motivating the academia and industry researchers to develop multi-channel diversity antenna. The antenna with spatial diversity is most prominent among other diversity techniques, such as pattern and polarization diversities, because it produces a wider spectrum signal. Additionally, it also provides higher-quality transmission/reception services and wide area coverage without any additional antenna spectrum [1], [2]. At the same time, there is an increasing interest in super wideband technology, as it covers multiple wireless bands within its broad frequency spectrum, thereby improving signal reliability, throughput, and radiation efficiency. Therefore, the spatial diversity antenna (SDA) with SWB technique is highly desirable to combat multipath complexities, pace the data transfer rates (>1 Gb/s), and improve the channel spectrum at both terminals (transmitter/receiver). Several SWB diversity antennas with miniaturized sizes have been designed over the past few years [3–7]. Three elliptical elements [3], a half-circular disc-shaped patch [4], a spade-shaped antenna [5], a feather-shaped radiator [6], and a hexagonal Koch-fractal radiator [7] have been examined for SWB applications. Further, to decouple the closely spaced antenna elements printed on the dielectric substrate, various structures have been introduced, for example, an anti-parallel placement [3], a corrugated T-shaped strip [4], a windmill-shaped [5], a diagonal metallic strip [6], and a meander line [7].

Regrettably, several unlicenced narrow bands such as Bluetooth (2.4 GHz), WiMAX-band (3.3–3.7 GHz), WLAN-band (5.15–5.85 GHz), and X-band (7.02–8.06 GHz) overlap with the SWB frequency spectrum which may create electromagnetic interference (EI). To suppress this EI issue, band-notched SWB antennas are needed. The various design methodologies have been carried out recently; for example, slots and slits (L, C, U, H-L-shaped) embedded on the antenna radiator or the ground structure [8–11], using electromagnetic bandgap (EBG) structure [12–14], and placing parasitic strips (resonators) near the feed line as well as on the radiator [15–17] are prominent nowadays.

Therefore, various diversity antennas with multi-band notched characteristics have been analyzed to immune the system from undesired bands [18–23]. A two-port circular SDA in [18] engraves two vertical ground slots to reduce the EI for the 5.9–7.1 GHz band. To enhance the isolation greater than 20 dB, an uneven E-shaped stub jointly with a mushroom-shaped EBG structure is used. An arrow-head-shaped antenna element loaded with two L-shaped, one U-shaped, and a couple of EBG structures is designed to obtain a quadruple band-notch feature in [19]. A rectangular strip is used to decouple the incoming signals between ports. Also, the orthog-

onally oriented self-complementary-antennas like quasi-elliptical-self-complementary [20], modified-elliptical-self-complementary [21], truncated-semi-elliptical-self- complementary [22], and sickle-shaped-self-complementary [23] are examined to attain SWB features with polarization diversity and better isolation (≥ 17 dB). Further, to acquire the band rejection (with center frequencies of 2.4, 3.5, 5.5, and 8.5 GHz), C, L-shaped slits [20–23], and CSRR [21–23] are etched on the radiator. Though the diversity systems stated in [18–23] are multi-band and have good isolation, despite that, many antennas have high coupling between notching structures [21–23] and moderate gain [19]. Also, the diversity performance indicators (Efficiency, DG, CCL, MEG, and TARC) in [19, 21–23] have not been analyzed, which are pivotal for diversity applications. Furthermore, most antennas have been designed for up to three notched bands and occupy ample space, which may not be compatible with modern IoT devices.

In this article, a tapered semicircular SWB-SDA with a quadruple band-notched feature is experimentally examined. The results show that the 2-element SDA operates from 1.88–30 GHz, however, the operation band for 4-element SDA is 1.65–30 GHz. Further, a periodic sinusoidal pattern-based WLDS is protruded from the CSGP to decouple the incoming waves between radiating ports. The four interfering bands across working frequencies, namely, Bluetooth (2.4 GHz), WiMAX (3.5 GHz), WLAN (5.5 GHz), and X-Band (7.5 GHz), are eliminated using meandering, OES, CSRR, and ESRR slots, respectively. The simulated and measured results for two-element (30 mm × 30 mm) and four-element (63 mm × 30 mm) are studied, which show stable radiation patterns, high peak gain, low ECC, and CCL.

2. Structural Layout of Two-Element SWB-SDA

The front and rear layouts of the proposed 2×2 band-notched SWB-SDA are configured in Fig. 1(a). The designed diversity system comprises two tapered semicircular radiators, with two 50-Ω tapered linear feedlines and a CSGP that provides wideband impedance (1.88–30 GHz) features. The two radiating elements are placed parallel in side-by-side orientation with an edge-to-edge separation of 5 mm to obtain size miniaturization and diversity performance. An OES slot along with a CSRR, an ESRR, and a meandering slot are introduced in each radiating element and a CSGP, respectively, to realize the four notch bands. As a consequence, the antenna achieves four notched bands in the frequency ranges of 2.1–2.7 (Bluetooth), 3.3–3.7 (WiMAX), 5–6 (WLAN), and 7.1–7.9 (X-Band) GHz. Further, a WLDS is protruded vertically from the ground plane between two antenna elements to decouple the incoming signals. The designed diversity system is manufactured on an FR4 substrate (having $\tan \delta = 0.02$, and $\epsilon_r = 4.4$) with a physical volume of 30 mm × 30 mm × 0.8 mm.

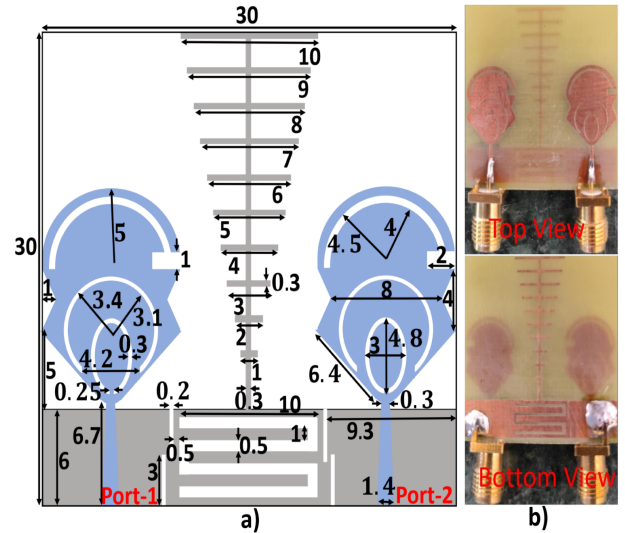**Fig. 1.** a) Layout and b) fabricated structure of the 2×2 band-notched SWB-SDA (all dimensions are in mm).
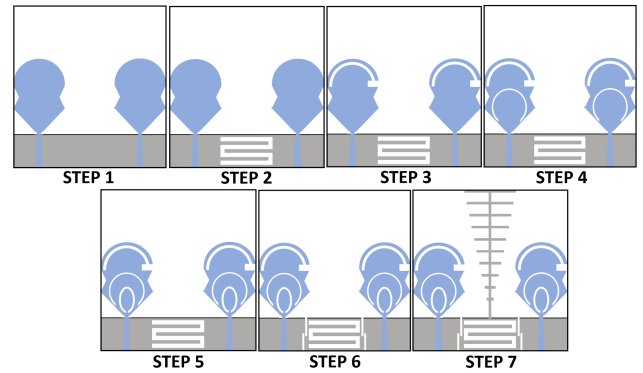

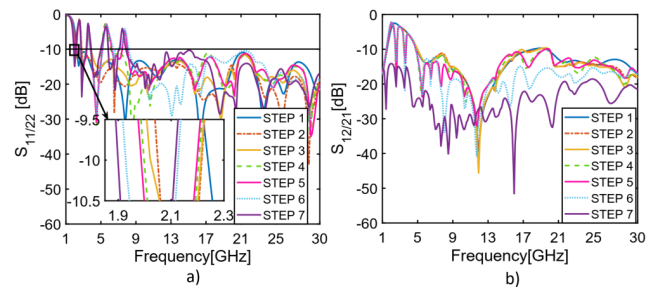**Fig. 2.** Evaluation of the proposed SWB-SDA.

Fig. 3. Simulated S-parameter: a) $S_{11/22}$ and b) $S_{12/21}$ vs. frequency variation of the proposed SWB-SDA.

3. Structural Evolution of Two-Element SDA

Figure 2 depicts the structural evaluation of the two-element MIMO system. The corresponding S-parameter graphs have been outlined in Fig. 3. STEP 1 consists of two identical reference antennas with a common ground plane (CGP), where each radiating element is composed of a semicircle and a rectangular element. This results in a wider impedance bandwidth in the band of 2.2–30 GHz, as depicted in Fig. 3. In STEP 2, a meandering slot of half-wavelength

($\lambda_g/2$) is imprinted on a CGP to eliminate the 2.4 GHz frequency band. Here λ_g is the guided wavelength and can be calculated as $\lambda_g = \lambda_0 \big/ \sqrt{0.5\,(\epsilon_r + 1)}$ [23] where λ_0 is the central notched frequency. Similarly, a quarter-wavelength OES slot ($\lambda_g/4$), a half-wavelength CSRR slot ($\lambda_g/2$), and a half-wavelength ESRR slot ($\lambda_g/2$) in STEPs 3, 4, and 5, respectively, are engraved on the radiator (portrayed in Fig. 2) to eliminate interfering bands at 3.5, 5.5, and 7.5 GHz. In the compact antenna structure, the CGP plays a vital role in obtaining antenna with good performance. However, it degrades the isolation between antenna ports due to interference between near-field and ground surface currents. Therefore, to diminish the mutual coupling, four similar rectangular slots oriented vertically are etched on the CGP in STEP 6, as presented in Fig. 2. Further, to improve the average port isolation higher than 24 dB, a WLDS is connected vertically to the ground plane in STEP 7. The WLDS consists of a periodic sinusoidal pattern, which can perturb the electromagnetic wave impedance properties continuously; as a result, the signals entering from port-1 do not interfere with port-2. It is noteworthy that WLDS not only enhances the isolation but also improves the percentage bandwidth from 175.2 to 176.4, as shown in Fig. 3.

The influence of the slots at the notched bands depicted in Fig. 4 is examined by the circulation of the current vector across the radiator and ground surface when port-1 is excited while port-2 is terminated with a 50-Ω load impedance. As shown in Fig. 4, the highly-dense currents are accumulated on the meandering (2.4 GHz), OES (3.5 GHz), CSRR (5.5 GHz), and ESRR (7.5 GHz) slots. However, the currents concentrated on each slot are opposite to the direction of the surface currents flowing across the remaining portion of the ground plane and patch, which nullifies the net radiation. Consequently, four notched bands with center frequencies of 2.4, 3.5, 5.5, and 7.5 GHz are acquired.

4. Study of Antenna Input Impedance Using Equivalent Circuit Layout

Input impedance characteristics of a wideband antenna can be realized by interlacing N-parallel RLC adjacent resonators, as shown in Fig. 5(a). Each RLC resonator has a distinct operating mode and provides a separate working frequency band to the antenna. Moreover, to mitigate the effect of substrate on the antenna performance, which is mainly owing to the large dielectric constant and gap between the radiator and ground plane, a capacitor (C_f) is added to the network (as given in Fig. 5(a)) [24]. To further understand the operating characteristics of the rejected bands, the graph of input impedance (real and imaginary) for reference structure (STEP 1) and proposed quadruple band-notched SWB-SDA (STEP 7) are outlined in Fig. 6. It is worth noting from Fig. 6(a) that the real and imaginary impedances of the basic SWB-SDA around 50 and 0 Ω respectively, resulting in proper impedance matching across the working bands.
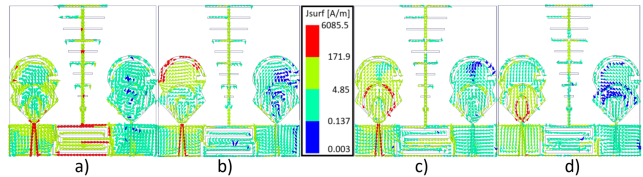

Fig. 4. Surface current distribution on the SWB-SDA at frequencies: a) 2.4 GHz, b) 3.5 GHz, c) 5.5 GHz, and d) 7.5 GHz.
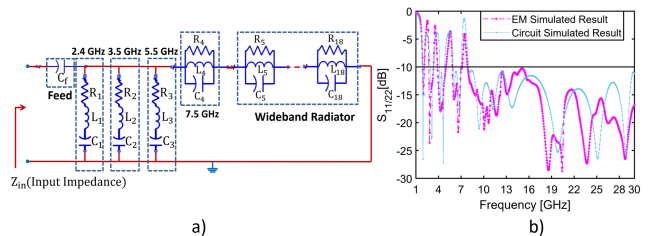

Fig. 5. a) Input impedance circuit topology for the quadruple band-notched SWB-SD antenna and b) circuit and EM simulated reflection coefficient versus frequency.
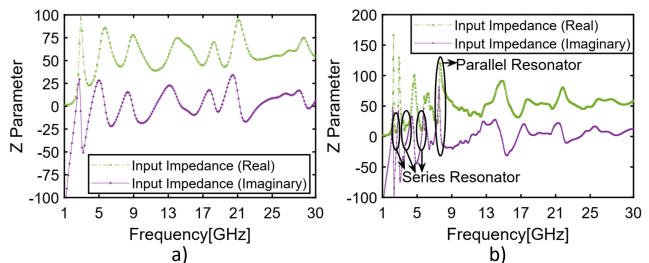

Fig. 6. a) Input impedance graph for the basic (Antenna 1) SWB-SD antenna and b) input impedance graph for the quadruple band-notched SWB-SD antenna.

However, the real part of the impedance of quadruple band-notched SWB-SDA (displayed in Fig. 6(b)) approaches minima at the notched center frequencies 2.4, 3.5, and 5.5 GHz while the imaginary curve is shifting from negative to a positive value, as a result exhibiting the series RLC resonating characteristics.

Furthermore, the real impedance at center frequency 7.5 GHz is large (> 100 Ω), while the imaginary impedance moves towards negative from positive value, displaying parallel RLC resonator behavior. The low impedance value in the series RLC network behaves as a short circuit. Nonetheless, the high impedance value in the parallel RLC network serves as an open circuit which leads to the antenna input impedance mismatch at the respective bands [17]. Corresponding to the impedance behavior, the equivalent circuit model of the proposed antenna is outlined in Fig. 5(a). One can observe from Fig. 5(a) that the C_f represents the antenna's feedline; three parallel-connected series RLC resonators denote the notched band centered at 2.4, 3.5, and 5.5 GHz, respectively. However, a band-notch centered at 7.5 GHz is represented by a parallel RLC network. In addition, the remaining 14 series connected parallel RLC networks represent the wideband radiator. The analytical input impedance expression of the intended quadruple notched band SWB-MIMO antenna for the constructed equivalent circuit model can be written as [25], [26]:

$$Z_{\text{in}}(\omega) \cong \frac{1}{j\omega \cdot C_{\text{f}}} + \frac{Z_{\text{s}} \cdot Z_{\text{a}}}{Z_{\text{s}} + Z_{\text{a}}} \qquad (1)$$

where,

$$Z_{\text{s}} = Z_{\text{s1}} \parallel Z_{\text{s2}} \parallel Z_{\text{s3}}, \qquad (2)$$

$$Z_{\text{a}} = \sum_{m=4}^{18} \frac{j\omega \cdot R_m \cdot L_m}{R_m \cdot (1 - \omega^2 \cdot L_m \cdot C_m) + j\omega \cdot L_m}. \qquad (3)$$

In (3), L_m, C_m, and R_m ($m = 4$–18) represent the inductor, capacitor, and resistor, respectively. The same equation can be further simplified to calculate the value of resonating elements (L_m, C_m, and R_m) while considering only the real part and expressed mathematically as [25]:

$$R_{\text{a}} = \sum_{m=4}^{18} \frac{R_m}{1 + R_m \cdot \left(2\pi f \cdot C_m - \frac{1}{2\pi f \cdot L_m}\right)}. \qquad (4)$$

However, to derive the frequency bandwidth equation of the series-type resonators (Z_{sk}, where $k = 1, 2, 3$) in Fig. 5(a), the resistance of series resonators (R_{sk}) with respect to R_k, L_k, C_k can be expressed as [27]:

$$R_{sk} = R_k + j\omega_{sk}L_k + \frac{1}{j\omega_{sk}C_k}. \qquad (5)$$

For a frequency adjacent to the resonant frequency ($\omega_{(s0)k}$) [27]:

$$\omega_{sk} = \omega_{(s0)k} + \Delta\omega_{sk}, \qquad (6)$$

$$\omega_{(s0)k} = \frac{1}{\sqrt{L_k C_k}}. \qquad (7)$$

By employing (6) and (7) in (5), the resistance of the series resonator (R_{sk}) can be modified as [27]:

$$\begin{aligned} R_{sk} &= R_k + \frac{1 - \omega_s^2 L_k C_k}{j\omega_{sk}C_k} \\ &= R_k + \frac{j}{\omega_{sk}C_k}(\Delta\omega_{sk}^2 + 2\omega_{(s0)k}\Delta\omega_{sk}) \cdot L_k C_k \\ &\approx R_k + j2L_k\Delta\omega_{sk}. \end{aligned} \qquad (8)$$

Equation (8) indicates that R_{sk} is equivalent to the total input impedance of a series network of R and $2L$.

The −3 dB operational bandwidth (BW) of the series-type resonators circuit (R_k, L_k, C_k) is approximately equal to twice the −3 dB BW of the series network of R and 2L, and can be mathematically expressed as [27]:

$$BW_{sk} = 2\frac{R_k}{2L_k} = \frac{R_k}{L_k}. \qquad (9)$$

The proposed circuit layout (as defined in Fig. 5(a)) has been authenticated by evaluating the series and parallel resonating parameters R_m, L_m, C_m (for $m = 1$–18) using (1)–(9). Further, the ADS software is used to construct the proposed circuit design. Parameters of the circuit design are optimized by tuning their value (as given in Tab. 1) to obtain the simulated frequency band consisting of quadruple notched bands.

The comparison of the reflection coefficient ($S_{11/22}$) curve for the circuit (ADS) and the EM (HFSS) simulation is outlined in Fig. 5(b), which exhibits a reasonably good agreement between both results.

Resonating mode (m = 1–18)	Resistance [Ω]	Inductance [pH]	Capacitance [pF]
feed	-	-	5.04
m = 1	6.44	17410.5	0.026
m = 2	10.4	23300.13	0.02
m = 3	3.07	175700.12	0.012
m = 4	141.24	132.405	0.14
m = 5	65.38	81.495	1.97
m = 6	47.77	141.435	2.281
m = 7	56.95	62.47	11.55
m = 8	45.68	115.625	10.31
m = 9	73.135	105.9	13.865
m = 10	54.56	114.42	5.345
m = 11	42.75	6.245	4.57
m = 12	78.41	156.27	2.81
m = 13	53.77	78.28	0.649
m = 14	67.78	146.26	0.59
m = 15	52.76	636.23	10.89
m = 16	52.89	472.33	5.785
m = 17	40.69	98.91	2.2
m = 18	46.27	26.48	1.32

Tab. 1. The extracted value of the optimized parameters from ADS software.

5. Results and Discussions

The proposed SWB-SDA is fabricated on an FR4 substrate by an LPKF etching machine (outlined in Fig. 1(b)) and tested the experimental results using an Anritsu S820E vector network analyzer. The measured and simulated graphs of the reflection coefficient ($S_{11/22}$) and transmission coefficient ($S_{12/21}$) for the intended antenna are depicted in Fig. 7(a). The measured outcomes show that the fabricated antenna can operate in the band of 1.88–30 GHz and has better average port isolation ($\geq$ 24 dB). It also demonstrates that the designed antenna has successfully produced the quadruple band-notched with impedance bandwidth ($S_{11/22}$) greater than −3 dB for Bluetooth, WiMAX, WLAN, and X-band. However, there are some minor discrepancies in the measurement results, perhaps owing to the manufacturing inadequacies, soldering imperfection, and connecting probes.

The measured and simulated realized peak gains of the intended 2-element for port-1 are displayed in Fig. 7(b). The realized peak gain varies linearly from 0.6–6.4 dBi over the working frequency (1.88–30 GHz); however, the gain drops are around −3, −3.5, −2.2, and −2 dBi at the notched bands of 2.4, 3.5, 5.5, and 7.5 GHz, respectively. Similarly, the simulated and measured efficiencies shown in Fig. 11(b) range between 80–92% in the operational band, whereas realized radiation efficiency is below 30% in the vicinity of a quadruple notched band.

The measured and simulated radiation characteristics in XY (E-plane) and XZ (H-plane) planes at frequencies 3.5, 9, 14, and 18 GHz for port-1 (considering symmetrical ports) are plotted in Fig. 8. The antenna performs a dumbbell-shaped pattern with a maximum gain along 0° (5.6 dBi) and 180° (6.4 dBi) for E-plane and an omnidirectional pattern for

$$\rho_{e_{12}} = \frac{\left\| \iint \left[XPR \cdot E_{\theta_1} E_{\theta_2}^* P_\theta + E_{\phi_1} E_{\phi_2}^* P_\phi \right] d\Omega \right\|^2}{\iint \left[XPR \cdot E_{\theta_1} E_{\theta_1}^* P_\theta + E_{\phi_1} E_{\phi_1}^* P_\phi \right] d\Omega \times \iint \left[XPR \cdot E_{\theta_2} E_{\theta_2}^* P_\theta + E_{\phi_2} E_{\phi_2}^* P_\phi \right] d\Omega} \tag{10}$$

H-plane at lower frequencies. On the contrary, the radiation pattern alters at higher frequencies due to an imbalance of current distribution around the radiating elements. Additionally, when the source signal is swapped from port-1 to 2, the patterns of the E and H-plane remain unchanged. The ratio between co- and cross-polarizations shows that the proposed antenna has a stable radiation pattern within the working frequency.
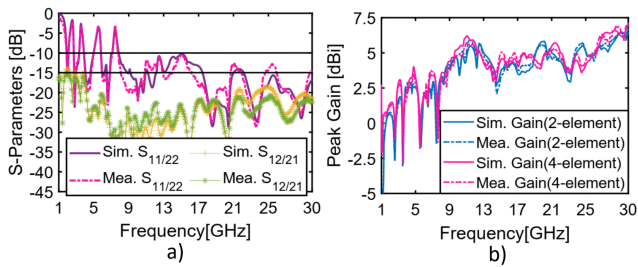

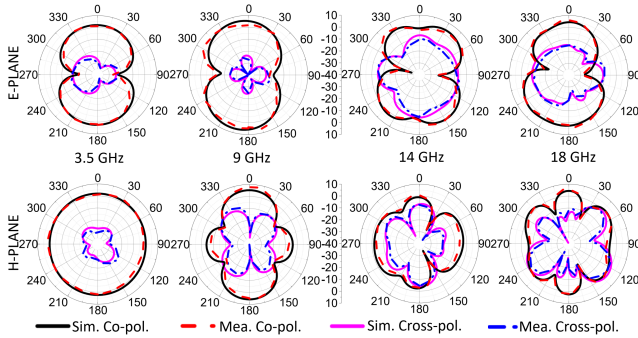**Fig. 7.** Simulated and measured results of proposed SWB-SDA: a) S-parameters and b) peak gain.

Fig. 8. Simulated and measured radiation patterns for E(XY) and H(XZ)-plane at: a) 3.5 GHz, b) 9 GHz, c) 14 GHz, and d) 18 GHz.
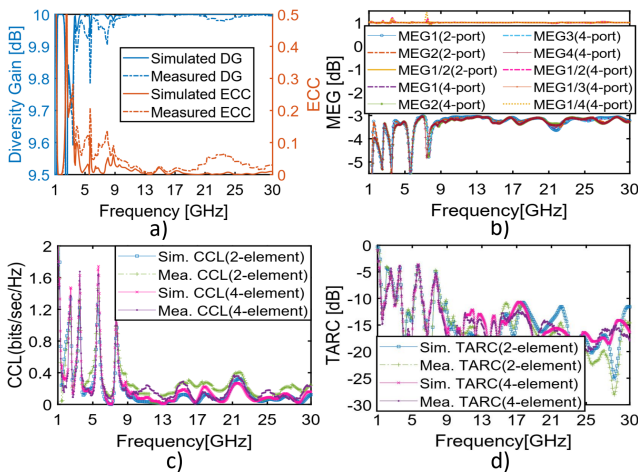

Fig. 9. Simulated and measured results for: a) ECC and DG, b) MEG c) CCL, d) TARC.

5.1 Performance Analysis of MIMO/Diversity Antenna

5.1.1 Envelop Correlation Coefficient (ECC) and DG

ECC measures the correlation between the field patterns of two antenna elements, and its value should have less than 0.5 for optimal diversity performance. The calculation of ECC in terms of radiation fields can be performed based on (10) [28].

Here, XPR states the cross-polarization power rate of the incident signal, E is the measure of θ and ϕ polarized electric field pattern, and P_ϕ and P_θ are the power distribution of the arriving waves in the ϕ and θ directions, respectively. ECC value should be zero for an uncorrelated MIMO performance, nonetheless can range between 0 to 0.5.

Diversity gain affirms the improvement in the diversity antenna compared to a single element and can be evaluated using ECC, given in (11) [9]. From Fig. 9(a), it is seen that the values of ECC and DG are around <0.07 and 10 dB, respectively, over the entire specified bandwidth, excluding the rejected bands, indicating that the proposed MIMO antenna has fairly well diversity among the antenna ports:

$$DG = 10\sqrt{1 - (ECC)^2}. \tag{11}$$

5.1.2 Mean Effective Gain (MEG) and Channel Capacity Loss (CCL)

MEG is a decisive parameter to characterize the MIMO performance for hazy conditions. It provides the relation between the total power accepted by the diversity antenna to the isotropic antenna in a multi-path scattering environment, and its ratio (MEG1/MEG2) for an uninterrupted diversity performance should be close to ±3 dB. The mathematical calculation of MEG for both the ports ($i, j = 1$ or 2) of the proposed SDA can be performed by using (12) [7]:

$$MEG_i = \left[1 - \sum_{j=1}^{2} \left\| S_{ij} \right\|^2 \right] \Big/ 2. \tag{12}$$

CCL is another MIMO performance indicator that shows the losses in the MIMO communication systems. For satisfactory data transmission, the desired value of CCL must be less than 0.4 bits/sec/Hz and can be computed using the following expressions [7]:

$$C_{\text{loss}} = -\log_2 \det \left(\psi_R \right) \tag{13}$$

where

$$\Psi_R = \begin{bmatrix} R_{11} & R_{12} \\ R_{21} & R_{22}, \end{bmatrix} \tag{14}$$

$$R_{mm} = 1 - \|S_{mm}\|^2 - \|S_{mn}\|^2, \tag{15}$$

$$R_{mn} = -\left(S_{mm}^* \cdot S_{mn} + S_{nm}^* \cdot S_{mn}\right). \tag{16}$$

Here S_{mm}^* and S_{nm}^* represent the complex conjugate of S_{mm} and S_{nm} respectively for $m, n = 1$ or 2.

The results of MEG and CCL of the 2-element MIMO system are outlined in Fig. 9(b) and (c). From the figure it is observed that the MEG ratio is unity, and the CCL curve is below 0.2 bits/sec/Hz within the specified frequency spectrum.

5.1.3 TARC

TARC is the square root of the ratio of total power reflected by the ports to the total power incident at the ports. Evaluation of TARC is performed using S-parameters as expressed in (17) [7]

$$TARC = \sqrt{\frac{\left\|S_{11} + S_{12}e^{j\theta}\right\|^2 + \left\|S_{21} + S_{22}e^{j\theta}\right\|^2}{2}} \tag{17}$$

where, θ varies between 0 and 2π. TARC is less than $-10\,\text{dB}$ as portrayed in Fig. 9(d), which demonstrates that the designed SDA delivers maximum radiated power to free space.

6. Four-Element SWB-Spatial Diversity Antenna

In the wireless radio frequency system, channel capacity, throughput, and reliability can be strengthened by increasing the number of radiating elements. The fabricated 4-element band-notched SWB-SDA structure is portrayed in Fig. 10(a), which is constructed by placing two similar elements adjacent to the original 2-element array on top of the substrate. Further, a wiggly line printed on the ground plane has also been extended to achieve high diversity between the antenna ports. The designed antenna array has a total physical volume of $30 \times 63 \times 0.8\,\text{mm}^3$. The measured and simulated graphs of the $S_{11/22}$ and $S_{12/21}$ for the 4-element SWB-SDA (only port-1 is excited while ports 2, 3, and 4 are matched with load impedance, i.e., $50\,\Omega$) are depicted in Fig. 10(b). It is observed that the proposed antenna has successfully eliminated the quadruple notched bands from the SWB frequency region with center frequencies of 2.4, 3.5, 5.5, and 7.5 GHz and has a larger operating bandwidth (from 1.65–30 GHz) than the 2-element array for $S_{11/22} \le -10\,\text{dB}$. Additionally, the average port isolation of the 4-element is higher than the 2-element. The measured and simulated realized peak gain (7 dBi) and radiation efficiency (85%) of the proposed 4-element for port-1 are displayed in Fig. 7(b) and Fig. 11(b), respectively.
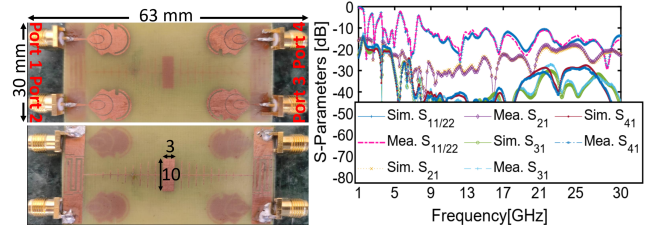

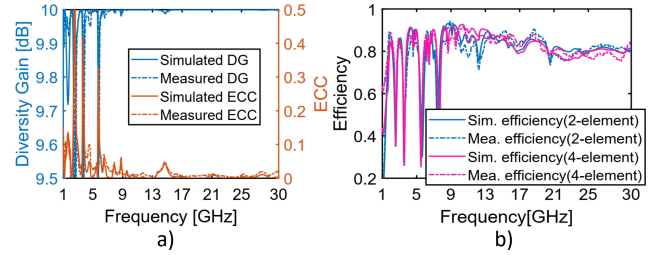**Fig. 10.** a) Fabricated 4×4 band-notched SWB-SDA configuration, b) simulated and measured S-parameters.

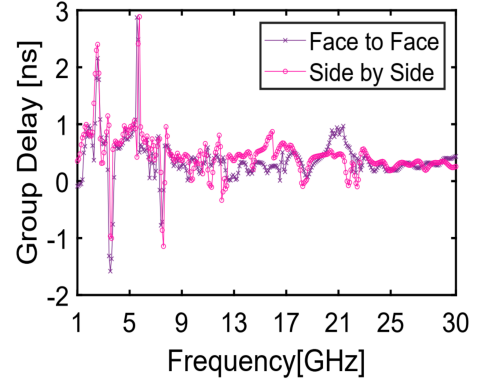**Fig. 11.** Measured and simulated results for: a) ECC & DG, and b) efficiency.

Fig. 12. Simulated group delay of the proposed quadruple band-notched SWB-SDA.

6.1 SDA Performance Parameter

The ECC and DG of the 4-element structure are outlined in Fig. 11(a). The measured and simulated results show that the ECC is below 0.06, while DG is close to 10 dB, outside the notched bands.

Similarly, Figures 9(b), (c), and (d) display the graphs of MEG, CCL, and TARC for 4-elements SDA. From Fig. 9(b), the MEG ratio is found to be unity for all the ports. On the other hand, the values of CCL and TARC are below 0.14 bits/sec/Hz and $-10\,\text{dB}$, respectively, indicating that the 4-element MIMO antenna performs better than the 2-element SDA.

Table 2 highlights the performance analysis of the proposed antenna (2 and 4-element) in contrast to existing wideband MIMO antennas. The antennas presented in [18,20–23] have only triple notched bands, while the antenna shown in [19] supports quadruple notch bands but at the cost of narrow bandwidth. Furthermore, most of the reported antennas have not examined the other essential parameters, such as CCL, TARC, efficiency, and MEG.

Ref.	Antenna Size [mm^2]	BW [GHz]	ISO [dB]	Ports	ECC	Band-notch	Peak Gain [dBi]	Rad. Eff. [%]
[18]	55.6×50.5	1.5–40	>20	2	0.03	1	7.6	-
[19]	43×34.9	3–10.7	>25	2	0.01	4	5	-
[This Work]	**30×30**	**1.88–30**	**>24**	**2**	**0.07**	**4**	**6.4**	**85**
[20]	52×52	1.25–40	>18	4	0.09	2	4.5	70
[21]	63×63	0.97–35	>17	4	0.01	2	5	-
[22]	63×63	1.3–40	>16	4	0.01	3	5.5	-
[23]	56×56	1.3–40	>22	4	0.03	3	7	-
[This Work]	**63×30**	**1.65–30**	**>25**	**4**	**0.06**	**4**	**7**	**85**

Tab. 2. Performance comparison with existing MIMO antennas.

7. Study of Time Domain Behavior

The group delay evaluates the pulse transition duration across the two radiators to analyze the distortion in the electromagnetic signal at the receiving end. It is analyzed by setting-up two similar antennas in side-by-side (SBS) and face-to-face (FTF) alignment in the far-field region at a distance of 30 cm from each other. An antenna with flat group delay (<1 nano sec) is preferred for ideal distortionless pulse transmission. Figure 12 shows that the group delay curves are within one ns for SBS and FTF arrangements, except at the notched bands. This exhibits that the phases are linear in the antenna far-field region resulting in distortionless transmission.

To further evaluate the peak magnitude of the cross-correlation between the received and source pulse (fifth derivative of Gaussian pulse), the system fidelity factor (SFF) is examined by utilizing the expression given below [29]

$$SFF = \max \left[\frac{\int_{-\infty}^{\infty} T_{\mathrm{x}}(t)\, R_{\mathrm{x}}(t+\tau)\, \mathrm{d}t}{\sqrt{\int_{-\infty}^{\infty} \|T_{\mathrm{x}}(t)\|^2 \mathrm{d}t \int_{-\infty}^{\infty} \|R_{\mathrm{x}}(t)\|^2 \mathrm{d}t}} \right]. \quad (18)$$

In (18), T_{x} and R_{x}, are transmitting (fifth derivative of Gaussian pulse) and receiving pulses, however, group delay is represented as τ. The mathematically evaluated results provide the SFF of 0.792 and 0.768 for FTF and SBS arrangements, respectively.

8. Conclusion

In this article, a tapered semicircular SWB-SDA with quadruple band-notched characteristics has been designed to implement two and four elements to operate from 1.88–30 GHz and 1.65–30 GHz, respectively. The quadruple notch bands at 2.4 GHz (Bluetooth), 3.5 GHz (WiMAX), 5.5 GHz (WLAN), and 7.5 GHz (X-band) were eliminated from the SWB frequency spectrum by loading the meandering, OES, CSRR, and ESRR slots, respectively. The measured and simulated results demonstrate the suitability of the proposed antenna for radar imaging, cognitive radio, military, and long-range RF applications. The proposed antenna has a stable radiation pattern, higher efficiency, high peak gain, low ECC, and CCL both for 2 and 4-element. However, with respect to bandwidth, isolation, peak gain, ECC, and CCL, the 4-element MIMO system outperforms the 2-element.

References

[1] KOOHESTANI, M., HUSSAIN, A., MOREIRA, A. A., et al. Diversity gain influenced by polarization and spatial diversity techniques in ultrawideband. *IEEE Access*, 2015, vol. 3, p. 281–286. DOI: 10.1109/ACCESS.2015.2421505

[2] GENG, J., ZIOLKOWSKI, R. W., WANG, K., et al. Dual CP polarization diversity and space diversity antennas enabled by a compact T-shaped feed structure. *IEEE Access*, 2019, vol. 7, p. 96284–96296. DOI: 10.1109/ACCESS.2019.2925396

[3] LIU, J., ESSELLE, K. P., HAY, S. G., et al. A compact superwideband antenna pair with polarization diversity. *IEEE Antennas and Wireless Propagation Letters*, 2015, vol. 12, p. 1472–1475. DOI: 10.1109/LAWP.2013.2287500

[4] ULLAH, H., RAHMAN, S. U., CAO, Q., et al. Design of SWB MIMO antenna with extremely wideband isolation. *Electronics*, 2020, vol. 9, no. 1, p. 1–12. DOI: 10.3390/electronics9010194

[5] YU, C., YANG, S., CHEN, Y., et al. A superwideband and high isolation MIMO antenna system using a windmillshaped decoupling structure. *IEEE Access*, 2020, vol. 8, p. 11567–11577. DOI: 10.1109/ACCESS.2020.3004396

[6] SINGHAL, S. Feather-shaped super wideband MIMO antenna. *International Journal of Wireless and Microwave Technologies*, 2021, vol. 13, no. 1, p. 94–102. DOI: 10.1017/S1759078720000549

[7] CHAUDHARY, A. K., MANOHAR, M. A modified SWB hexagonal fractal spatial diversity antenna with high isolation using Meander line approach. *IEEE Access*, 2021, vol. 10, p. 10238–10250. DOI: 10.1109/ACCESS.2022.3144850

[8] KANG, L., LI, H., WANG, X., et al. Compact offset microstrip-fed MIMO antenna for band-notched UWB applications. *IEEE Antennas and Wireless Propagation Letters*, 2015, vol. 14, p. 1754–1757. DOI: 10.1109/LAWP.2015.2422571

[9] CHANDEL, R., GAUTAM, A. K., RAMBABU, K. Tapered fed compact UWB MIMO-diversity antenna with dual band-notched characteristics. *IEEE Transactions on Antennas and Propagation*, 2018, vol. 66, no. 4, p. 1677–1684. DOI: 10.1109/TAP.2018.2803134

[10] CHEN, Z., ZHOU, W., HONG, J. A Miniaturized MIMO antenna with triple band-notched characteristics for UWB applications. *IEEE Access*, 2021, vol. 9, p. 63646–63655. DOI: 10.1109/ACCESS.2021.3074511

[11] TANG, Z., WU, X., ZHAN, J., et al. Compact UWB-MIMO antenna with high isolation and triple band-notched characteristics. *IEEE Access*, 2019, vol. 7, p. 2169–3536. DOI: 10.1109/ACCESS.2019.2897170

[12] ABBAS, A., HUSSAIN, N., LEE, J., et al. Triple rectangular notch UWB antenna using EBG and SRR. *IEEE Access*, 2020, vol. 9, p. 2508–2515. DOI: 10.1109/ACCESS.2020.3047401

[13] PENG, L., WEN, B. J., LI, X. F., et al. CPW fed UWB antenna by EBGs with wide rectangular notched-band. *IEEE Access*, 2016, vol. 4, p. 9545–9552. DOI: 10.1109/ACCESS.2016.2646338

[14] MODAK, S., KHAN, T., LASKAR, R. H. Penta-notched UWB monopole antenna using EBG structures and fork-shaped slots. *Radio Science*, 2020, vol. 55, no. 9, p. 1–11. DOI: 10.1029/2019RS006983

[15] LI, Z., YIN, C., ZHU, X. Compact UWB MIMO Vivaldi antenna with dual band-notched characteristics. *IEEE Access*, 2019, vol. 7, p. 28696–38701. DOI: 10.1109/ACCESS.2019.2906338

[16] KUMAR, S., KUMAR, R., VISHWAKARMA, R. K., et al. An improved compact MIMO antenna for wireless applications with band-notched characteristics. *AEU-International Journal of Electronics and Communications*, 2018, vol. 90, p. 20–29. DOI: 10.1016/j.aeue.2018.04.008

[17] LUO, S., CHEN, Y., WANG, D., et al. A monopole UWB antenna with sextuple band-notched based on SRRs and U-shaped parasitic strips. *AEU-International Journal of Electronics and Communications*, 2020, vol. 120, p. 1–9. DOI: 10.1016/j.aeue.2020.153206

[18] SAXENA, G., JAIN, P., AWASTHI, Y. K. High diversity gain super-wideband single band-notch MIMO antenna for multiple wireless applications. *IET Microwaves, Antennas & Propagation*, 2020, vol. 14, no. 1, p. 109–119. DOI: 10.1049/iet-map.2019.0450

[19] MODAK, S., KHAN, T. A slotted UWB-MIMO antenna with quadruple band-notch characteristics using mushroom EBG structure. *AEU - International Journal of Electronics and Communications*, 2021, vol. 134, p. 1–6. DOI: 10.1016/j.aeue.2021.153673

[20] RAHEJA, D. K., KUMAR, S., KANAUJIA, B. K. Compact quasi-elliptical-self-complementary four-port super-wideband MIMO antenna with dual band elimination characteristics. *AEU - International Journal of Electronics and Communications*, 2020, vol. 114, p. 1–10. DOI: 10.1016/j.aeue.2019.153001

[21] RAHEJA, D. K., KANAUJIA, B. K., KUMAR, S. Low profile four-port super-wideband multiple-input-multiple-output antenna with triple band rejection characteristics. *International Journal of RF and Microwave Computer-Aided Engineering*, 2019, vol. 29, no. 10, p. 1–13. DOI: 10.1002/mmce.21831

[22] KUMAR, P., UROOJ, S., ALROWAIS, F. Design of quad-port MIMO/diversity antenna with triple-band elimination characteristics for super-wideband applications. *Sensors*, 2020, vol. 20, no. 3, p. 1–13. DOI: 10.3390/s20030624

[23] KUMAR, P., UROOJ, S., MALIBARI, A. Design and implementation of quad-element super-wideband MIMO antenna for IoT applications. *IEEE Access*, 2020, vol. 8, p. 226697–226704. DOI: 10.1109/ACCESS.2020.3045534

[24] ORAIZI, H., REZAEI, B. Dual-banding and miniaturization of planar triangular monopole antenna by inductive and dielectric loadings. *IEEE Antennas and Wireless Propagation Letters*, 2013, vol. 12, p. 1594–1597. DOI: 10.1109/LAWP.2013.2293615

[25] CHU, Q. X., YANG, Y. Y. A compact ultrawideband antenna with 3.4/5.5 GHz dual band-notched characteristics. *IEEE Transactions on Antennas and Propagation*, 2008, vol. 56, no. 12, p. 3637–3644. DOI: 10.1109/TAP.2008.2007368

[26] ZHANG, K., WANG, T., CHENG, L. L. Analysis of band-notched UWB printed monopole antennas using a novel segmented structure. *Progress In Electromagnetics Research C*, 2013, vol. 34, p. 13–27. DOI: 10.2528/PIERC12082401

[27] ZHU, F., GAO, S., HO, A. T., et al. Multiple band-notched UWB antenna with band-rejected elements integrated in the feed line. *IEEE Transactions on Antennas and Propagation*, 2013, vol. 61, no. 8, p. 3952–3960. DOI: 10.1109/TAP.2013.2260119

[28] WANG, L., DU, Z., YANG, H., et al. Compact UWB MIMO antenna with high isolation using fence-type decoupling structure. *IEEE Antennas and Wireless Propagation Letters*, 2019, vol. 18, no. 8, p. 1641–1645. DOI: 10.1109/LAWP.2019.2925857

[29] SINGHAL, S., SINGH, A. K. CPW-fed hexagonal Sierpinski super wideband fractal antenna. *IET Microwaves, Antennas & Propagation*, 2016, vol. 10, no. 15, p. 1701–1707. DOI: 10.1049/iet-map.2016.0154

About the Authors . . .

Abhishek Kumar CHAUDHARY is currently pursuing the Ph.D. in Electronics and Communication Engineering at the Indian Institute of Information Technology Senapati, Manipur, India. His research interests include super wideband and MIMO/diversity antenna for future electronics handheld devices.

Murli MANOHAR received the Ph.D. degree in Electronics and Electrical Engineering from the Indian Institute of Technology Guwahati, India in April 2015. He is presently working as an Assistant Professor in the Dept. of Electronics and Communication Engineering, Indian Institutte of Information Technology Manipur, India. His main research area is in antenna and RF engineering with a focus on SWB printed monopole antenna.